





# Land Subsidence in Villahermosa Tabasco Mexico, Using Radar Interferometry

Zenia Pérez-Falls  and Guillermo Martínez-Flores  

Instituto Politécnico Nacional, Centro Interdisciplinario de Ciencias Marinas, Av. Instituto Politécnico Nacional S/N, Col. Playa Palo de Santa Rita, 23096 La Paz, B.C.S., México  
zperezf1600@alumno.ipn.mx, gmflores@ipn.mx

**Abstract.** Land subsidence is a geological phenomenon that consists of the gradual sinking of the earth's crust and can damage to the urban infrastructure and the population. This phenomenon is caused, among other factors, by the overexploitation of aquifers and the excessive extraction of hydrocarbons. The Synthetic Aperture Differential Radar Interferometry (DInSAR) technique has been used since the late 1990s to detect deformations on the ground, including subsidence in higher spatial and temporal coverage compared to traditional methods such as geodesic, instrumental, GPS at a sensitivity of mm/year. The Villahermosa city, Tabasco, concentrates 512 oil wells in an area of 10 km<sup>2</sup> located in the northwest of the town. The DInSAR technique was implemented to quantify the subsidence of the land in the Villahermosa city. Twenty-eight SAR images from the Sentinel-1A satellite from 2014 to 2018 were used. These images were processed with SNAP, the SNAPHU algorithm, and QGIS. Maximum land subsidence of 4 cm/year (2014–2015) was obtained in the southwest region in an area of 327 ha. For the period 2016–2018, the land subsidence was 15 cm/year in an extension of 6,232 ha.

**Keywords:** DInSAR · Sentinel-1A · SAR · Urban nucleus

## 1 Introduction

Subsidence is considered a risk factor in urban areas. Subsidence is a type of land collapse characterized by near-vertical deformation or settlement of earth materials [1]. The study of subsidence in urban areas is essential, where the damages caused can become considerable, being a significant risk for the urban infrastructure [2].

Surfaces that can be affected by subsidence can occupy areas from a few square meters to thousands of square kilometers [3].

Land subsidence has been calculated using traditional geodetic techniques such as leveling, Global Positioning Implementation Systems (GPS), as well as instrumental methods. Also, methodologies have been implemented with synthetic aperture radars (SAR), such as interferometry (InSAR) and differential interferometry (DInSAR), which began to be developed from the 1990s.

Many investigations have been carried out to obtain the deformation of the terrain associated with various causes such as water extraction [4, 5], mining exploitation [6, 7],

geothermal fields [8, 9], river delta [10, 11], anthropic influence [12, 13], hydrocarbon extraction [14, 15], among others.

This last technique has become a useful and essential tool in remote sensing as it can estimate both spatial and temporal surface movements due to ground subsidence [16]. DInSAR has a series of advantages compared to traditional geodetic and instrumental techniques, such as its wide spatial coverage in different areas, such as urban areas, and being able to be used as monitoring services at lower costs [2]. The possibility of the DInSAR technique to detect subsidence makes it viable to monitor almost any earth structure subject to displacement [17].

## 1.1 SAR Images and DInSAR

SAR images are used to implement a conventional technique in which the terrain is illuminated with electromagnetic waves of microwave frequency [9, 17]. The wave round-trip time and the signal amplitude reflected by objects in the ground are used to determine the distances from the sensor to the ground and generate a two-dimensional image of the interest area [18]. The bright regions in a radar image represent a large amplitude of the returned wave energy, which depends on the surface slope and the roughness and dielectric characteristics of the surface material [18]. Amplitude is a measure of the target's reflectivity, while the phase encodes changes in the surface, and a term proportional to the range of the target [17, 18].

The InSAR technique began to be implemented in the late 1990s. It consists of exploiting the information contained in the phase of at least two SAR images taken from slightly different points in the same area. The images are processed to relate the difference between their distances to the same point on the ground with the scene topography [9, 19]. InSAR uses the phase information in two SAR images to determine the phase difference between each pair of points in the corresponding images, thus producing an interferogram.

Differential SAR interferometry (DInSAR) is a variant of InSAR. It is an image processing technique that allows the generation of terrain displacement maps and the calculation of relative coherence [20]. It is also used to detect and measure movements so small that the topography component must be discarded [17].

The primary sources of noise and error of the InSAR technique are the loss of coherence due to the high intensity of the vegetation, the lack of temporal correlation, the topographic residuals due to the precision of the Digital Elevation Model (DEM) and the atmospheric factors such as temperature and variations of water vapor in the atmosphere [21].

## 2 Study Area

The study area corresponds to Villahermosa city in the Centro municipality, Tabasco, with an area of 61,232 ha. The Villahermosa city, the capital of Tabasco, is in the Southeast region of the country at 92° 55' west longitude and 17° 59' north latitude, corresponding to the physiographic region of the Southern Gulf Coastal Plain sub-province Tabasco Plains and Swamps [23] (see Fig. 1).

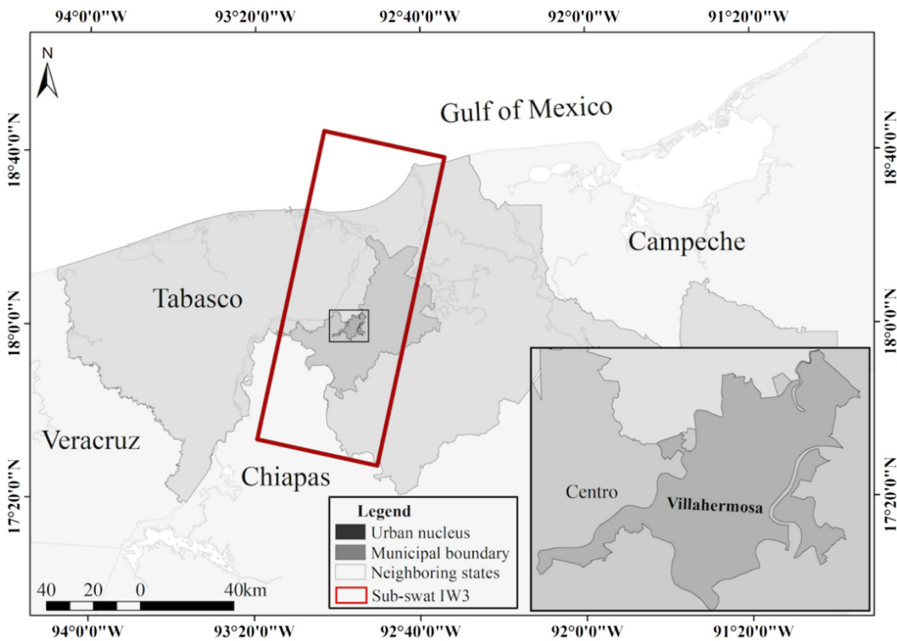


**Fig. 1.** Study area location. The red rectangle shows the sub-swath IW3, corresponding to the scene of a Sentinel-1A satellite image with descending orbit. (Color figure online)

This city is in the floodplain of the Grijalva River, being the most important urban settlement in Tabasco, due to the development in recent decades of hydrocarbon extraction as the main economic activity [23]. The oil boom in the 1960s was a determining factor for urban growth, beginning in the second half of the 20th century, as it became the main economic activity. This boom led to an increase from 23,947 (first half of the 20th century) to 297,268 inhabitants [23, 24].

Regarding lithology, it is based on sandstone and sedimentary rocks from the Cenozoic era [25]. A predominance of soils formed in the alluvial quaternary is found. The most abundant soils are gleysols characterized by a clay texture, and slow drainage, formed on unconsolidated materials.

The area belongs to the Hydrological Region Grijalva-Usumacinta, the largest and most flowing region in Mexico. It has a wide lake system with a high density of bodies of water. Hydrological conditions contribute to the area being subject to flooding [22] due to the high precipitation regime. The topography characterizes the area with few slopes, as well as the low permeability of the soils [22, 23]. Furthermore, in the region there is an intense activity of hydrocarbon extraction. Villahermosa has a density of 512 wells per 10 km<sup>2</sup> in the northwest of the area.

The climate is warm humid with abundant rains in summer, according to the Köppen classification, with average temperatures of 27.5 °C. Average annual rainfall of 1,992 mm [22].

On the other hand, the changes in land use became more notable at the same time as the discoveries of hydrocarbon deposits. In the period 2000–2008, the noteworthy loss of

arboreal vegetation (1,624 ha) and wetlands (213 ha) began to be evident, while grassland (540 ha) and urban areas (1,334 ha) continued to increase. This trend of land-use change has been maintained (2008–2020), reaching 15,697 ha [23].

### 3 Data and Methods

#### 3.1 Data

The SAR images used to implement the DInSAR technique in this work correspond to the Sentinel-1 satellite. These satellites operate in the *Interferometric Wide swath* (IW) imaging band mode and acquire data with a 250 km range at a spatial resolution of  $5 \times 20$  m. IW captures three sub-swaths using the *Terrain Observation with Progressive Scans SAR* (TOPSAR) acquisition principle. IW products that are *Single Look Complex* (SLC) contain one image per sub-band and one for polarization channel, for a total of three images (single polarization) or six (dual polarization) in a single product [26]. Sentinel-1 images are available from its start of operation in 2014 (Sentinel-1A) until today.

Twenty-eight images from the Sentinel-1A satellite from 2014 to 2018 of the European Space Agency (obtained from <https://search.asf.alaska.edu>) were used.

The images were selected considering the following: 1) The perpendicular baseline between the image pair should be as small as possible, while smaller (closer to zero), the contribution of the topography component that is subtracted from the interferometric process is less. 2) The time interval between images, the shorter it is (less than 1,000 days), the less deco-relationship there will be for the scale of the movement that is to be measured [26, 27]. Using a DEM with good precision improves the quality of the phase by subtracting the topographic component. Sub-swath IW3 corresponding to Sentinel-1A descending orbit was processed.

Table 1 shows the image dates used for DInSAR processing. From these, 25 interferograms were formed.

#### 3.2 Methods

The terrain's deformation was obtained with the implementation of a series of processes (see Fig. 2) that make up the DinSAR technique. Sentinel-1A images were processed with SNAP software (*Sentinel Application Platform*) to generate the interferograms. The interferograms were then unwrapped to obtain the interferometric phase with the SNAPHU algorithm (*Statistical-cost, Network-flow Algorithm for Phase Unwrapping*). Then, the terrain deformation rate was determined using SNAP software. For the cartographic output of the deformation, visualization, and interpretation, QGIS was used. Next, DInSAR processing will be described in more detail.

**Image Co-registration.** For interferometric processing, two or more images must be registered together. One image is selected as master and the others as slaves with dates after the first. The pixels in the slave images must be aligned with the master. This procedure ensures each pixel (of both images) belongs to the same location on the ground (in range and azimuth) [26].

**Table 1.** Sentinel-1A images used to form the interferometric pairs. Date: image acquisition date, T: images type (M: master, S: slave),  $B_L$ : perpendicular baseline,  $B_T$ : temporal baseline (frame: 99, path: 530, descending orbit).

Date	T	$B_L$	$B_T$	Date	T	$B_L$	$B_T$
2014-10-24	M			2017-04-11	S	29	192
2015-01-04	S	33	72	2017-05-05	M		
2015-05-04	S	11	192	2017-06-22	S	44	252
2015-06-21	S	-73	240	2017-10-08	S	18	360
2015-07-15	S	-159	264	2017-10-20	S	8	372
2015-08-08	S	-108	288	2017-11-01	S	30	384
2015-09-01	S	-112	312	2017-11-25	S	25	408
2015-10-19	S	-115	336	2017-12-07	S	-61	420
2016-10-13	M			2017-12-19	S	31	432
2016-11-30	S	44	48	2018-03-01	S	43	504
2016-12-24	S	16	72	2015-10-19	M		
2017-02-22	S	-15	132	2016-10-13	S	-5	361
2017-03-06	S	-98	144	2015-05-04	M		
2013-03-18	S	-35	156	2017-02-10	S	-33	648

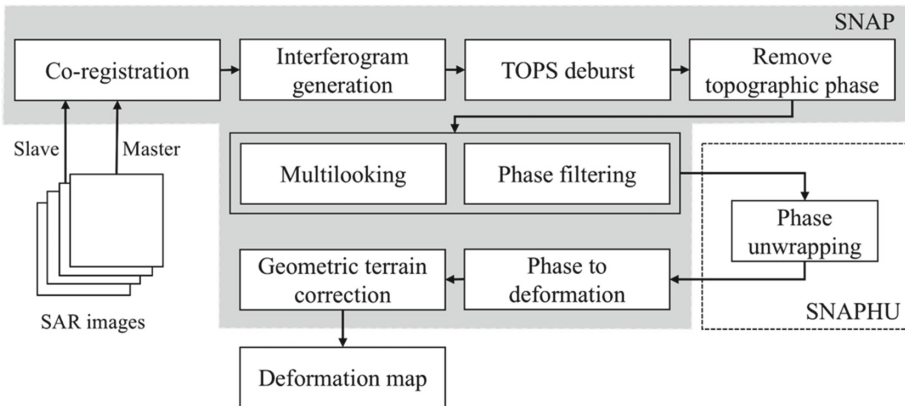


**Fig. 2.** Methodological scheme showing the procedures performed to implement the DInSAR technique and the software (SNAP, SNAPHU) used in each stage.

**Interferogram Formation.** The interferogram is formed by cross-multiplying the master image with the slave conjugate complex. The amplitudes of both images are multiplied

while the phases are subtracted to form the interferogram [26]. Therefore, the interferogram is the phase variation between the two images and is related to the differences in object distances [19].

The integral DInSAR equation to calculate the interferometric phase, where M is the master image, and S is the slave image (1) [19]:

$$\begin{aligned}\Delta\varphi_{D\_Int} &= \Delta\varphi_{Int} - \Delta\varphi_{Topo\_simu} \\ &= \Delta\varphi_{Displ} + \Delta\varphi_{Topo\_res} + \Delta\varphi_{Atms} - \Delta\varphi_{Orb_S} - \Delta\varphi_{Orb_M} + \Delta\varphi_{Noise} + 2k\pi\end{aligned}\quad (1)$$

Where:

$\Delta\varphi_{Int}$ : Interferometric component.

$\Delta\varphi_{Topo\_simu}$ : Simulated topographic component, which implicitly contains a flat earth component.

$\Delta\varphi_{Topo\_res}$ : Component of the residual topographic error (RTE).

$\Delta\varphi_{Atm}$ : Atmospheric phase component in the acquisition time of each image.

$\Delta\varphi_{Orb}$ : Phase component due to orbital errors of each image.

$\Delta\varphi_{Noise}$ : Phase noise.

$2k\pi$ : Phase ambiguity (the result of the wrapped interferogram of  $\Delta\varphi_{D\_Int}$ ).

The quality of the terrain deformation data obtained using the DInSAR technique depends on the quality of the differential interferometric phase [9].

The interferometric bands represent a  $2\pi$  cycle of phase change. They appear on an interferogram as colored bands, where each represents a relative range difference of half the sensor wavelength. Relative ground motion can be calculated by counting the stripes and multiplying by half the wavelength [26].

The parameter called coherence ( $0 < \text{“coherence”} < 1$ ) is calculated to evaluate the interferometric phase. If the coherence is close to zero, it means that the scene is uncorrelated, and therefore the interferogram is noisy. Values close to 1 indicate high correlation, low noise on the interferogram, and a high-quality strain map [9]. Values less than 0.3 indicate that the phase estimates are too noisy to be used [27].

**TOPS Deburst.** Sentinel-1 images (due to the way they operate), present some bursts that cause noise and distortions to extract information. It is necessary to carry out this process TOPS deburst to eliminate such bursts [26].

**Remove the Topographic Phase.** The topographic phase's contribution is removed (Eq. 1) to disregard the components that do not contribute to the phase to obtain terrain deformation. For this, a well-known DEM is used to simulate the reference DEM based interferogram, in this case, the DEM SRTM1 (*Shuttle Radar Topography Mission*) [26, 27].

**Multilooking.** It is done to decrease the noise of the interferogram. It consists of obtaining the average of the pixels in each direction (several looks) in the interferograms. Interferograms of approximately  $14\text{ m}^2$  were obtained [9, 28].

**Phase Filtering.** Subsequently, the Goldstein filter was performed, a pre-processing technique that reduces noise from the interferometric phase, facilitating its development in terms of precision [29]. By completing this filtering, the interferometric strips are accentuated and become sharper.

**Phase unwrapping.** In the interferogram, the interferometric phase is ambiguous and is only known within  $2\pi$ . The phase must first be unwrapped to separate the interferometric phase from the topographic height [26].

Starting from the phase and amplitude information (see Fig. 3), the phase unwrapping is performed using the SNAPHU algorithm. SNAPHU is a statistical cost network flow algorithm for phase development developed at Stanford University [30] as a complement to the SNAP software developed by ESA and freely available. The focus of radar interferometry in this step is to work with the two-dimensional relative phase signal, the modulus  $2\pi$  of the absolute phase signal (unknown). In this sense, the biggest drawback is the wrapped phase given in an interval of  $(-\pi, \pi)$  and, on the other hand, the phase unwrapping, being more complex due to its non-linearity and non-singularity [31].

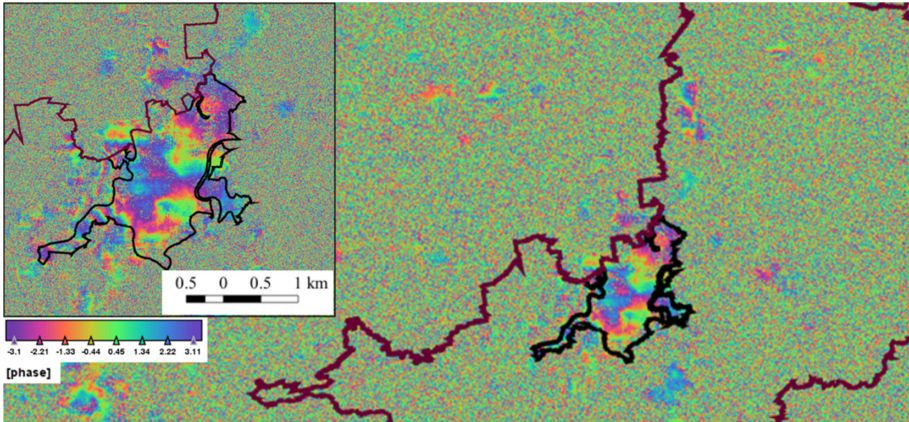


**Fig. 3.** Filtered interferogram. Sub-swath IW3 corresponding to the pair of images on 2014-10-13 and 2015-01-04. The polygon in brown shows the limits of Municipality Centro and the black one, the Villahermosa city boundary. (Color figure online)

**Phase to deformation conversion.** In this step, the unwrapped interferometric phase is converted to heights. The phase of several discrete heights is calculated and compared to the actual phase of the interferogram to determine the height. An external DEM is used as a reference (SRTM 1 Arc-Second) [29–31].

**Geometric correction of the terrain.** Geometric correction or geocoding converts a slope range image or terrain range geometry to a map coordinate system. Besides, the use of a DEM is required to correct the mentioned distortions [31].

**Land deformation map.** As the last step, the terrain deformation map is obtained in cm/year, and this is taken to the Geographic Information System for better visualization and interpretation of this [9, 26, 28, 30].



## 4 Results and Discussion

Six of the 25 interferograms formed (see Fig. 4) and their respective coherence maps obtained from 2014 to 2018 (see Fig. 5) are represented. The thresholds obtained in the coherence maps were very similar, ranging from 0.01 to 0.992, with an approximate mean of 0.25 to 0.3.

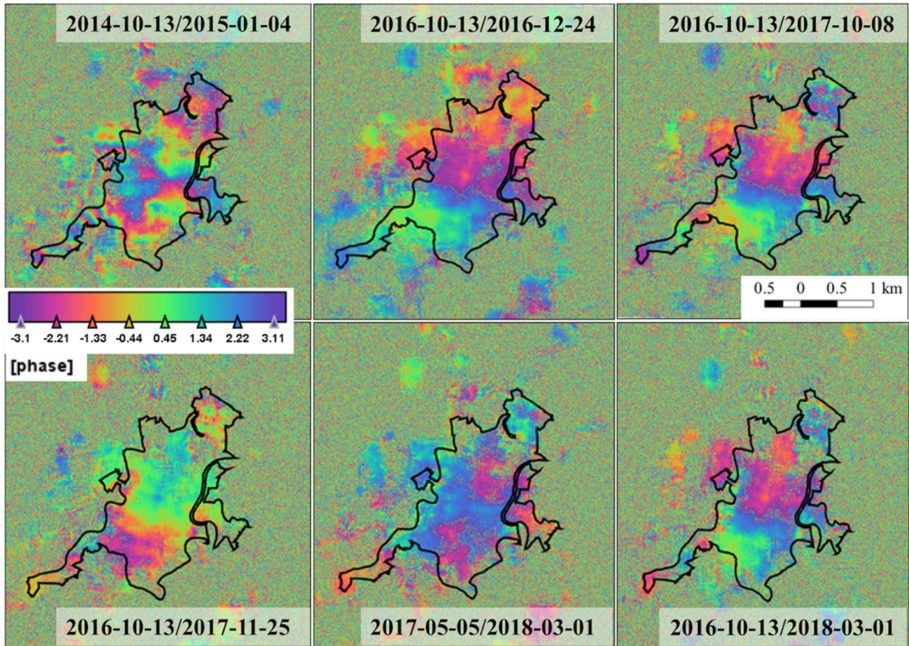


**Fig. 4.** Flattened interferograms of the city of Villahermosa that contain information on topography and terrain deformation for the period 2014-10-13 to 2018-03-01.

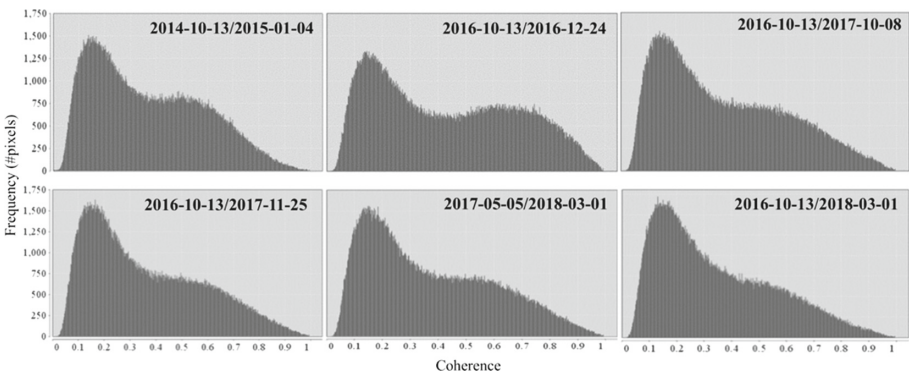


**Fig. 5.** Histograms of the coherence parameter corresponding to the city of Villahermosa covering the period 2014-10-13 to 2018-03-01.



Acceptable results were obtained from the 25 processed interferograms in the image pairs shown in Fig. 4. The contribution of those, as mentioned earlier, temporal and atmospheric distortions, were detected in the interferograms. In an interferogram, the deformation pattern is shown with a color cycle. Each stripe represents a change in the distance from the satellite to the ground, which is equal to half the radar wavelength. When the number of stripes visible on the interferogram is multiplied by half the wavelength, a relative displacement of the points can be estimated. Since the images used are from descending orbit, this is represented on the interferograms by positive values (see Fig. 4). Negative values in the interferograms correspond to sinks, while positive values represent the uprisings [32]. Interference stripes with the same color within the cycle represent the same relative deformation.

The average coherence of the interferometric phase for processed images was between 0.3 and 0.40 (see Fig. 5). The highest coherence values belong to interferograms of 2016-10-13 to 2016-12-24 and 2016-10-13 to 2018-03-01 with 0.40 and 0.35 thresholds, respectively. Thresholds values greater than 0.3, indicate areas with similar reflection characteristics. On the other hand, the areas with values less than 0.3 may be due to a longer time interval between the two image acquisitions, the temporal, spatial geometric decorrelation between the two SAR images [14].

Despite the temporal decorrelations caused by the acquisition of images at different year seasons and with a temporality of 648 days, the deformation results were consistent (3 to 15 cm/year from 2014-10-13 to 2018-03-01).

From 2014-10-13 to 2015-01-04, the city of Villahermosa had a sinking rate of 4 cm/year. From 2016-10-13 to 2018-03-01, the subsidence rate was 15 cm/year. The lowest subsidence values corresponded to the interferograms with a smaller temporal baseline. The areas affected by the sinking phenomenon increased from 327 ha from 2014 to 2015, to 6,232 ha from 2014 to 2018. Urban expansion and the continued exploitation of hydrocarbon wells contribute to this increase in the sinking rate from 2014 to 2018 in the city of Villahermosa (see Fig. 6).

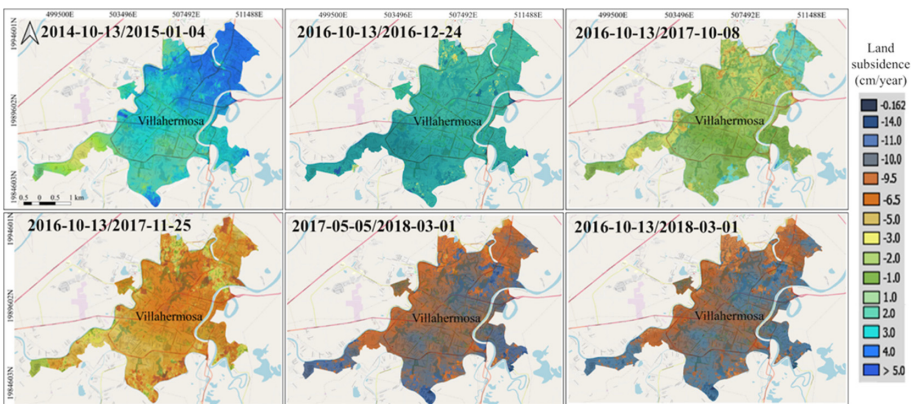


**Fig. 6.** Deformation of the land obtained in the city of Villahermosa for the period 2014-10-13 to 2018-03-01.

## 5 Conclusions and Future Work

The traditional DInSAR technique that obtains the deformation of the terrain from pairs of SAR images is viable for measuring and quantifying the evolution of the subsidence in urban areas at different periods. From 2014-10-13 to 2015-01-04, subsidence in the city of Villahermosa had a sinking rate of 4 cm/year. For the period from 2016-10-13 to 2018-03-01, the subsidence rate increased to 15 cm/year. The lowest subsidence values corresponded to the interferograms with the smallest time scale. Atmospheric and temporal distortions contributed to the erroneous development of interferograms. These led to incoherent interferometric phases to obtain the terrain deformation. The areas affected by the subsidence phenomenon increased from 327 ha (2014-2015) to 6,232 ha (2016-2018).

This work is part of an ongoing investigation on subsidence in the Tabasco and Campeche coastal plain. As future work, control points will be obtained in the field, as well as from the INEGI geodetic network, to validate the obtained results. Since there have been no previous studies to monitor subsidence in this region, it is necessary to quantify it to prevent and reduce the region's vulnerability to this phenomenon and other associated ones, such as floods and coastal erosion.

**Acknowledgments.** The authors would like to thank the Interdisciplinary Center of Marine Sciences of the National Polytechnic Institute (CICIMAR-IPN) for the support to carry out this work (through the project SIP-20195187 *Coastal subsidence assessment in the Mexican states of Tabasco and Campeche using DInSAR*). Thanks also to the three anonymous reviewers for their valuable comments, and to Alaska Satellite Facility Distributed Active Archive Center (ASF DAAC) for providing access to Sentinel-1A imagery.

## References

1. Keller, E.A., Blodgett, R.H.: *Riesgos Naturales. Procesos de la Tierra como riesgos, desastres y catástrofes*. 1st edn. Pearson Prentice Hall, Madrid (2004)
2. Tomás, R., Herrera, G., Delgado, J., Peña, F.: Subsistencia del terreno. *Enseñanza de la Ciencia de la Tierra* **17**(3), 295–302 (2009)
3. Vázquez, N.J., de Justo J.L.: La subsistencia en Murcia. Implicaciones y consecuencias en la edificación. In: COPOT, pp. 1–260, Murcia, España (2002)
4. Dávila-Hernández, N.A., Madrigal-Uribe, D.: Aplicación de interferometría radar en el estudio de subsistencia en el Valle de Toluca, México. *Rev. Cien. Espaciales* **8**(1), 294–309 (2015)
5. Riel, B., Simons, M., Pontl, D., Agram, P., Jolivet, R.: Quantifying ground deformation in the los angeles and santa ana coastal basins due to groundwater withdrawal. *Water Resour. Res.* **54**, 3557–3582 (2018)
6. Hay-Man, A., Ge, L., Du, Z., Wang, S., Ma, Ch.: Satellite radar interferometric for monitoring subsidence induced by longwall mining activity using Radarsat-2, Sentinel-1 and ALOS-2 data. *Appl. Earth Obs. Geoinform.* **61**, 92–103 (2017)
7. Temporim, F.A., Gama, F.F., Mura, J.C., Paradella, W.R., Silva, G.G.: Application of persistent scatterers interferometry for surface displacements monitoring in N5E open pit iron mine using TerraSAR-X data, in Carajás Province, Amazon region. *Braz. J. Geol.* **47**(2), 225–235 (2017)

8. Liu, F., et al.: Inferring geothermal reservoir processes at the Raft River geothermal field, Idaho, USA, through modeling InSAR-measured surface deformation. *J. Geophys. Res. Solid Earth* **123**, 3645–3666 (2018)
9. Sarychikhina, O., Glowacha, E., Suárez, F., Mellors, R., Hernández, R.: Aplicación de DInSAR a los estudios de subsidencia en el Valle de Mexicali. *Boletín de la Sociedad Geológica Mexicana* **63**(1), 1–13 (2011)
10. Higgins, S.A., Overeem, I., Steckler, M.S., Syvitski, J.P.M., Seeber, L., Akhter, S.H.: InSAR measurements of compaction and subsidence in the Ganges-Brahmaputra Delta, Bangladesh. *J. Geophys. Res. Earth Surf.* **119**, 1768–1781 (2014)
11. Saleh, M., Becker, M.: New estimation of Nile Delta subsidence rates from InSAR and GPS analysis. *Environ. Earth Sci.* **78**(6), 1–12 (2019)
12. Jones, A.E., An, K., Blom, R.G., Kent, J.D., Ivins, E.R., Bekaert, D.: Anthropogenic and geologic influences on subsidence in the vicinity of New Orleans, Louisiana. *J. Geophys. Res. Solid Earth* **121**, 3867–3887 (2016)
13. Cianflone, G., Tolomei, C., Brunori, C.A., Dominici, R.: InSAR time series analysis of natural and anthropogenic coastal plain subsidence (Southern Italy). *Remote Sens.* **7**, 16004–160023 (2015)
14. Arenas, I., Hernández, B., Royero, G., Cioce, V., Wildermann, E.: Detección de subsidencia por efecto de extracción petrolera aplicando la técnica DInSAR en Venezuela. *Rev. Mapp.* **28**(195), 8–26 (2019)
15. Ketelaar, G., et al.: Integrated monitoring of subsidence due to hydrocarbon production: consolidating the foundation. *Int. Assoc. Hydrol. Sci.* **382**, 117–123 (2020)
16. Herrera, G., et al.: Advanced DInSAR analysis on mining areas: La Union case study (Murcia, SE Spain). *Eng. Geol.* **90**, 148–159 (2007)
17. Silllerico, E., Marchamalo, M., Rejas, J.G., Martínez, R.: La técnica DInSAR: bases y aplicación a la medición de subsidencias del terreno en la construcción. *Informes de la Construcción* **62**(519), 47–53 (2010)
18. Bürgmann, R., Rosen, P.A., Fielding, E.: Synthetic aperture radar interferometric to measure earth surface and its deformation. *Earth Planet Sci. Lett.* **28**, 169–209 (2000)
19. Crosetto, M., Monserrat, O., Cuevas-González, M., Devanthéry, N., Crippa, B.: Persistent scatterer interferometry: a review. *ISPRS J. Photogram. Remote Sens.* **115**, 78–89 (2016)
20. Li, Z., Zou, W., Ding, X., Chen, Y., Liu, G.: A quantitative measure for the quality of InSAR interferograms based on phase differences. *Photogram. Eng. Remote Sens.* **70**(10), 1131–1137 (2004)
21. Constantini, F., Ruescas, A.B.: Estimación de la subsidencia en el área de Ostrava (República Checa) utilizando datos ERS SAR con técnicas de Interferometría Diferencial. *Teledetección: Agua y desarrollo sostenible*. In: XIII Congreso de la Asociación Española de Teledetección, pp. 545–548, Teledetección: Agua y desarrollo sostenible, España (2009)
22. Galindo, A.A., Ruiz A.S., Morales, H.A., Sánchez, L., Carrizales, E., Villegas P.C.: Atlas de Riesgos del Municipio de Centro. H. Ayuntamiento Constitucional de Centro, Tabasco. In: *Servicios Integrales de Ingeniería y Calidad SA de CV*, pp. 43–67, México (2015)
23. Palomeque, M.A., Galindo, A., Sánchez, A.L., Escalona, M.J.: Pérdida de humedales y vegetación por urbanización en la cuenca del río Grijalva, México. *Investigaciones Geográficas* **68**, 151–172 (2017)
24. Capdepont-Ballina, J.L., Marín-Olán, P.: La economía de Tabasco y su impacto en el crecimiento urbano de la ciudad de Villahermosa (1960-2010). *Revista LiminaR Estudios Sociales y Humanísticos* **12**(1), 144–160 (2014)
25. INEGI: Síntesis de Información Geográfica del Estado de Tabasco, (Digital). Aguascalientes, México, pp. 25–32 (2001)
26. Meyer, F.: Sentinel-1 InSAR processing using the Sentinel-1 toolbox. In: *Adapted from Coursework Developed in Alaska Satellite Facility*, pp. 1–21 (2019)

27. Ferretti, A., Monti-Guarnieri, A., Prati, C., Rocca, F.: InSAR Principles: Guidelines for SAR Interferometry Processing and Interpretation TM-19, pp. 1–63. ESA, France (2007)
28. Seppi, S.: Uso de Interferometría Diferencial para monitorear deformaciones del terreno en la comuna de Córdova, provincia de Bolzano, Italia. Grado de Máser en aplicaciones espaciales de alerta y respuesta temprana a emergencias. Universidad Nacional de Córdova, p. 32 (2016)
29. Golstein, R.M., Warner, C.L.: Radar interferogram filtering for geophysical applications. *Geophys. Res. Lett.* **25**(21), 4035–4038 (1998)
30. Chen, C.W., Zebker, H.A.: Phase unwrapping for large SAR interferograms: statistical segmentation and generalized network models. *IEEE Trans. Geosci. Remote Sens.* **18**(40), 338–351 (2002)
31. Guerrero, C.A., Hernández, P.A.: Determinación de un modelo digital de elevación a partir de imágenes de radar Sentinel-1 usando interferometría SAR. In: Proyecto curricular de Ingeniería Catastral y Geodesia, pp. 45–110, Bogotá, Colombia (2017)
32. Hanssen, R.F.: Radar Interferometry. Data Interpretation and Error Analysis. Remote sensing and Digital Image Processing. 2nd edn. Kluwer Academic Publishers, The Netherlands (2002)